ISSN 1063-7729, Astronomy Reports, 2017, Vol. 61, No. 9, pp. 805–819. © Pleiades Publishing, Ltd., 2017.
Original Russian Text © V.G. Eselevich, M.V. Eselevich, I.V. Zimovets, I.N. Sharykin, 2017, published in Astronomicheskii Zhurnal, 2017, Vol. 94, No. 9, pp. 793–807.

Evidence for Shock Generation in the Solar Corona in the Absence of Coronal Mass Ejections

V. G. Eselevich[1*], M. V. Eselevich[1], I. V. Zimovets[2,3,4], and I. N. Sharykin[1,2]

[1] *Institute of Solar–Terrestrial Physics, Siberian Branch of the Russian Academy of Sciences, Irkutsk, 664033 Russia*

[2] *Institute for Space Research, Russian Academy of Sciences, Moscow, 117997 Russia*

[3] *State Key Laboratory of Space Weather, National Space Science Center of Chinese Academy of Sciences, Beijing, China*

[4] *International Space Science Institute, Beijing, China*

Received December 22, 2016; in final form, February 20, 2017

Abstract—The solar event SOL2012–10–23T03:13, which was associated with a X1.8 flare without an accompanying coronal mass ejection (CME) and with a Type II *radio burst*, is analyzed. A method for constructing the spatial and temporal profiles of the difference brightness detected in the AIA/SDO UV and EUV channels is used together with the analysis of the Type II radio burst. The formation and propagation of a region of compression preceded by a collisional shock detected at distances $R < 1.3\,R_\odot$ from the center of the Sun is observed in this event ($R_\odot$ is the solar radius). Comparison with a similar event studied earlier, SOL2011–02–28T07:34 [1], suggests that the region of compression and shock could be due to a transient (impulsive) action exerted on the surrounding plasma by an eruptive, high-temperature magnetic rope. The initial instability and eruption of this rope could be initiated by emerging magnetic flux, and its heating from magnetic reconnection. The cessation of the eruption of the rope could result from its interaction with surrounding magnetic structures (coronal loops).

DOI: 10.1134/S1063772917080030

1. INTRODUCTION

Shocks are among the most common and interesting phenomena in the Universe. Shocks are conventionally divided into two types, according to their excitation mechanism: piston and explosive. Piston shocks are continually subject to the effect of their pistons as they propagate. Explosive shocks are generated due to transient increases in the total pressure, and propagate without any piston effects, leading to their rapid decay. The decay rate of a shock depends on the parameters of the ambient medium. In plasmas, the total pressure is the sum of the thermal and magnetic pressures.

The excitation of piston shocks is associated with coronal mass ejections (CMEs) [2–5], and flares accompanying such ejections can result in the excitation of explosive shocks [6–8]. Shocks propagating in the corona are manifest as Type II radio bursts at the fundamental frequency F and its harmonic $H \approx 2F$ [9, 10]. The temporal drift of F and H from higher to lower frequencies is related to the velocity of the shock-front propagation and the electron-density profile in the ambient plasma.

A method for the identification and direct detection of shock fronts has been develope [11, 12], to distinguish between the two types of shock when both a CME and a flare are observed. The physical basis for this method is the concept of perturbed zones [13] moving ahead of CMEs, which result from the CME's interaction with the unperturbed solar wind. In this case, the CME itself is the piston. Measurements of shock-front widths indicate that the energy-dissipation mechanism in shock fronts changes from collisional to collisionless, depending on the distance from the center of the Sun [14].

The first attempt to use this method for the direct detection of shock fronts is described in [15], including a joint analysis of spatially resolved sources of Type II radio bursts detected by the Nançay radio heliograph [16]. Analysis of the event SOL2010–11–03T12:07, whose second harmonic H was split into two components with close frequencies f_1 and f_2, led to the detection and identication of the fronts of the piston and explosive shocks attributed to the

*E-mail: esel@iszf.irk.ru

CME formation for the first time [15]. A similar analysis applied to the CME observed in SOL2010–06–13T05:30 likewise enabled the detection and identification of the fronts of the piston and explosive shocks [17].

As a rule, Type II radio bursts are accompanied by CMEs. However, a number of events have been observed in which Type II radio bursts, probably generated by flares, were observed without CMEs [18]. An event of this sort (SOL2011–02–28T07:34) was first studied in detail in [1]. The frequency drift of the Type II radio burst was attributed to the propagating shock. No methods for the direct detection of shock fronts were used. This analysis led to the conclusion that the flare was not directly responsible for the shock, whose excitation was instead attributed to the rapid expansion and then deceleration of a coronal magnetic loop. In this case, the transient effect exerted on the coronal plasma by the magnetic piston is responsible for the shock formation in the absence of a CME; the decaying shock front then propagates similarly to an explosive shock.

The aim of our present study is to investigate in detail the solar event SOL2012–10–23T03:13 (which, like SOL2011–02–28T07:34, displayed no CMEs but did display a Type II radio burst) by applying this method for the direct detection of shock fronts, accompanied by a joint analysis of the Type II radio burst. We will also compare our results with the conclusions drawn in [1] for SOL2011–02–28T07:34.

2. DATA AND PROCESSING METHODS

We used the AIA/SDO data [19] (EUV and UV images of the 94 Å–1700 Å channels[1]) for our analysis. The time resolution of this instrument is about 12 s, and the outer edge of its field of view is located at a distance of 1.3–1.4 $R_\odot$ from the center of the Sun.

We used difference images to study the region of compression and the associated shock in time and in various directions relative to its propagation axis. The EUV and UV images present the running difference brightness $\Delta P_R = P(t_2) - P(t_1)$, where $P(t_2)$ and $P(t_1)$ are the brightnesses of two images nearest to each other in time. In some cases, these images were also represented in the form of the difference brightness $\Delta P = P(t) - P(t_0)$, with a fixed initial time t_0 that preceded the start of the event, and with $t > t_0$.

Regions of enhanced brightness, which are probably associated with enhanced pressure (which we will further refer to as the region of compression), usually have shapes resembling a circular arc (see Fig. 1d), with its center located at the origin of the flare, denoted in Fig. 1a as the point O. The distance from the solar center to the point O determined in the direction of its positional angle PA is denoted R_C. The angle PA is measured counterclockwise from the north pole (see Fig. 1a). To construct the profile and correctly deduce the size of shock fronts in the difference brightness images, we constructed distributions of the difference brightness $\Delta P(r)$ for various angles α relative to the axis of the motion of the region of compression of the CME (relative to the PA) and for various times (the angle α increases counterclockwise, see Fig. 1a). The distance r is measured from the center O. The distances R to the solar center and r are related as $R = (R_C^2 + r^2 + 2rR_C\cos\alpha)^{1/2}$. Thus, we chose distributions $\Delta P(r)$ for our study that were directed approximately along the normal to the region of compression and the shock front moving ahead of it.

3. ANALYSIS OF THE EVENT SOL2012–10–23T03:13 OBSERVED IN THE "COLD" 211 Å CHANNEL

SOL2012–10–23T03:13 was associated with an X1.8 X-ray flare, which started near the eastern limb with heliographic coordinates S13E58 at about 03:13 UT. The flare was observed in both the UV and EUV bands, at least from 1700 Å to 94 Å. According to SOHO LASCO/C2 and C3[2] and STEREO-A and STEREO-B SECCHI/COR2[3] data, the absence of CMEs was among the most interesting features of this event, although a Type II radio burst was detected (http://www.e-callisto.org/).

Let us consider the progress of SOL2012–10–23T03:13 first in the comparatively "cold" ($T \approx 2 \times 10^6$ K) 211 Å channel and then in the "hotter" ($T \approx 10^7$ K) 131 Å channel. Though the AIA/SDO CCD arrays were overexposed at the location of the flare, distorting the detected brightness, it was still possible to attempt an analysis of the event dynamics. In addition to the structure St1 detected at the flare origin (the point O in Fig. 1a), the two arc structures St2 and St3 participating in the flare process became visible after $t = 03:14:37$ UT; these two structures moved a bit from the center of the Sun and then stopped, decreasing their brightness (these processes will be studied in more detail below, see Figs. 2–6). The second process that is clearly visible in the images is the appearance of the arc structures St3, St4, St5, and St6 with larger radii (larger sizes), which encompass the structures St1 and St2 at $t >$

[1] http://www.lmsal.com/get_aia_data/

[2] http://cdaw.gsfc.nasa.gov/CME_list/

[3] http://secchi.nrl.navy.mil/cactus/

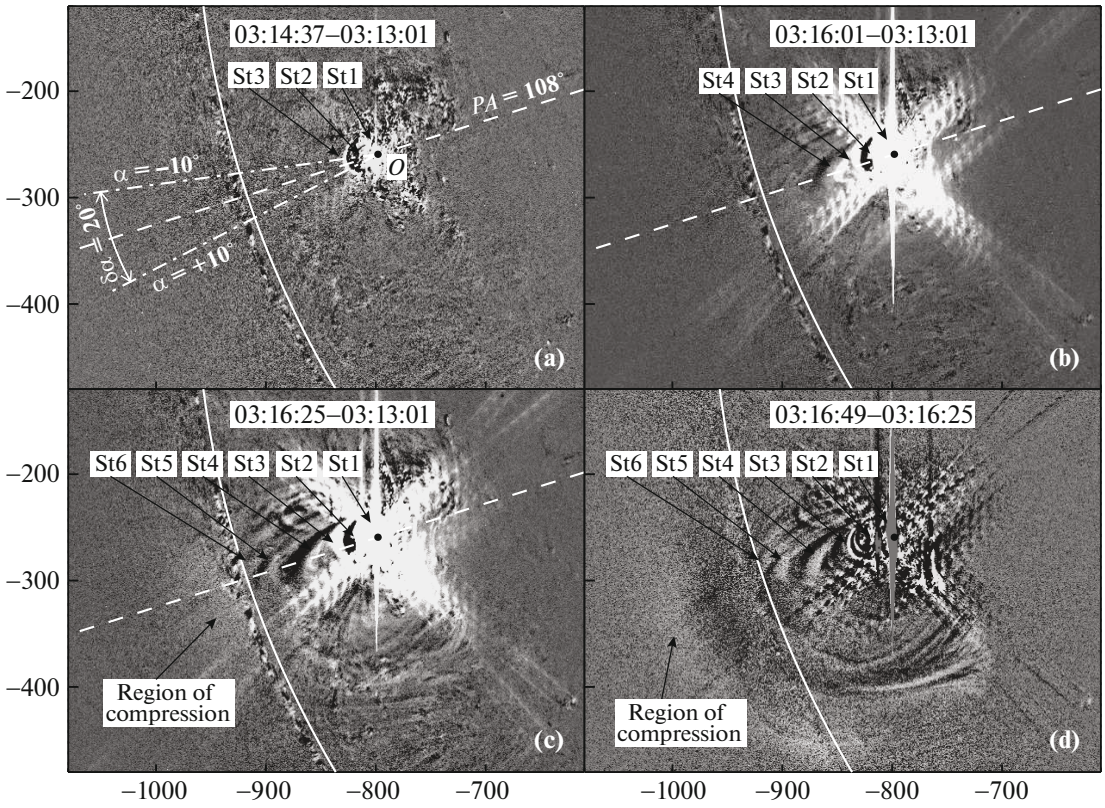

Fig. 1. AIA/SDO 211 Å images of (a)–(c) the difference brightness at successive times starting from $t_0 = 03:13:01$ UT and (d) the running difference brightness for SOL2012–10–23T03:13. The axes indicate solar coordinates in arcseconds.

03 : 15 : 13 UT. A region of compression ahead of these structures, whose leading front we interpreted as a shock, becomes visible after 03 : 16 : 25 UT (see Fig. 1c). This region is clearly visible as a region of enhanced brightness in the running difference-brightness image at 03 : 16 : 49 UT (see Fig. 1d).

To study this process in more detail quantitatively, we constructed distributions of the difference brightness $\Delta P = P(t) - P(t_0)$ (with $t_0 = 03:13:01$ UT) as functions of the distance r from the point O. These distributions were constructed along the direction $\alpha = 0°$ relative to $PA = 108°$, and were averaged over an angle $\delta\alpha = 20°$ (see Fig. 1a). Figure 2 presents these distributions as radial functions $\Delta P(r)$.

The brightness enhancement of the structure St1 located near the point O ($r = 0$) began about $t =$ 03 : 14 : 13 UT, just after the flare (hollow triangles in Fig. 2a). The brightness and width of St1 then sharply increase, while its position remains almost unchanged (hollow diamonds in Fig. 2a). The arc structure St2 rapidly appears at $r \approx 0.006\ R_\odot$, with its maximum brightness at $t = 03:14:49$ UT (filled circles in Fig. 2a). At $t = 03:15:13$ UT, this structure shifted to $r \approx 0.015$–$0.017\ R_\odot$ (diamonds in Fig. 2a), then remained fixed with a constant brightness (hollow and filled circles and pluses in Fig. 2b). During the interval between $t = 03:15:13$ UT and 03 : 16 : 25 UT, the arc structure St3 appeared at $r \approx 0.035\ R_\odot$, reached its maximum brightness, and then sharply decreased (diamonds in Fig. 2a, circles and pluses in Fig. 2b). The brightness of the arc structure St4 increased sharply at $r \approx 0.057\ R_\odot$ at $t = 03:16:01$ UT (filled circles in Fig. 2b), then decreased by almost an order of magnitude. However, the positioin of St4 remained almost constant (see Figs. 2c and 2d). The positions of the arc structures St5 and St6 also remain constant.

At the same time, the formation of a region of compression moving away from the Sun is observed immediately in front of the structure St6 (shown by the slanted shading in Figs. 2c and 2d). To analyze the formation of the region of compression after its appearance at $t = 03:15:13$ UT in more detail, we jointly considered the distributions of the difference brightness ΔP and of the running difference brightness ΔP_R for five successive times starting from $t =$ 03 : 15 : 13 UT.

Figure 3 presents these distributions for the same parameters as those used in Fig. 2. The formation

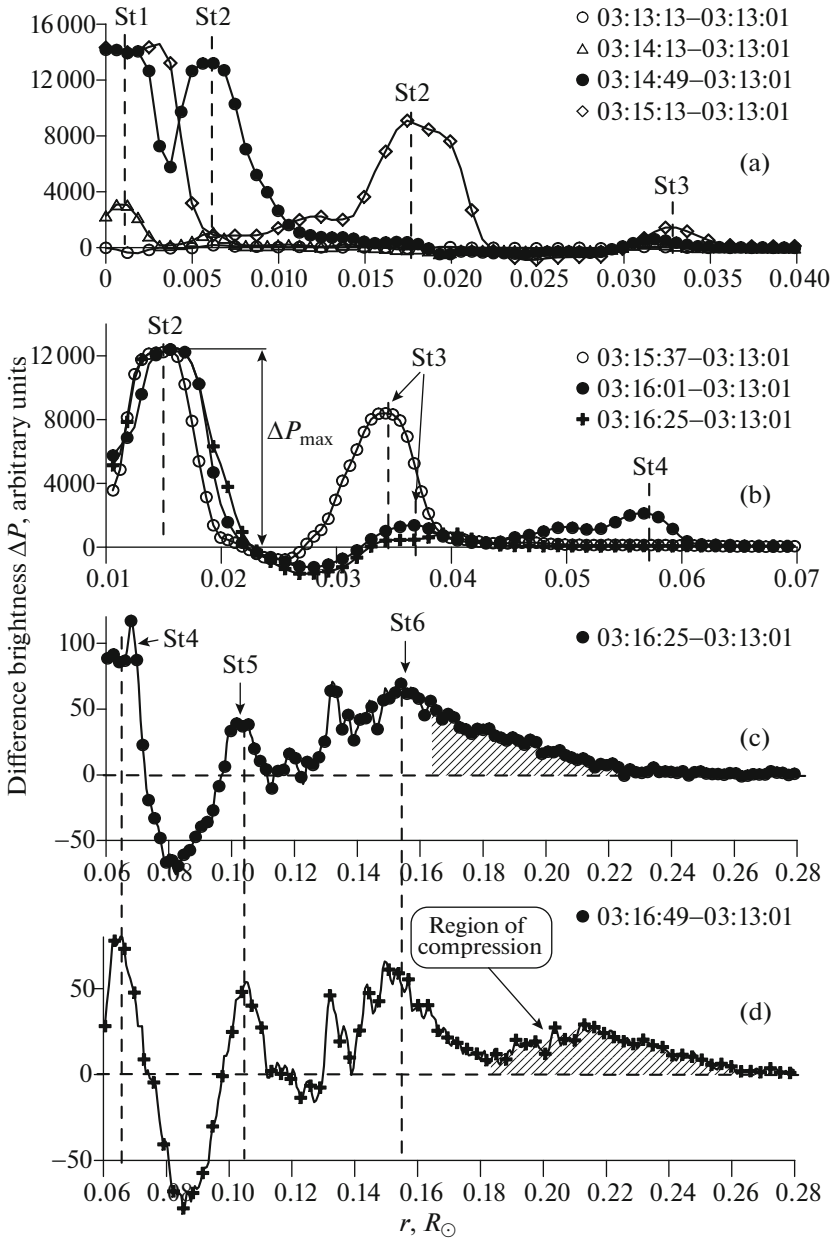

Fig. 2. AIA/SDO difference brightness $\Delta P(r)$ determined for SOL2012–10–23T03:13 in the 211 Å channel at successive times, indicated. The distributions were constructed along the direction $\alpha = 0°$ from the initial point O ($PA = 108°$, $R_C = 0.87\ R_\odot$), with angular averaging over $\delta\alpha = 20°$.

of the region of compression at $t = 03:15:37$ UT looks almost identical in the profiles for ΔP and ΔP_R (shown in Figs. 3b1 and 3b2 by the slanted shading). However, at the following time $t = 03:16:01$ UT, the formation of the shock front in the leading portion of the region of compression (gray in Fig. 3c2) is reliably seen in the ΔP_R profile, but not the ΔP profile (see Fig. 3c1). A similar situation is observed at other succeeding times (see Figs. 3d1 and 3e1). This can be explained by the fact that the curves of the difference brightness ΔP simultaneously describe changes in the brightness profile and the position of the observed structure. On the contrary, the running difference brightness ΔP_R describes the profile of the moving leading area, i.e., the shock front. It is difficult to distinguish the shock front via a visual analysis of the running difference image (see Fig. 1d). As the region of compression (shown by slanted shading in Figs. 3b1–3e1 and Figs. 3b2–3e2) moved through the structures St4, St5, and St6, the brightnesses and profiles of these structures changed (see the ΔP variations shown in Figs. 2c and 2d and Figs. 3a1–

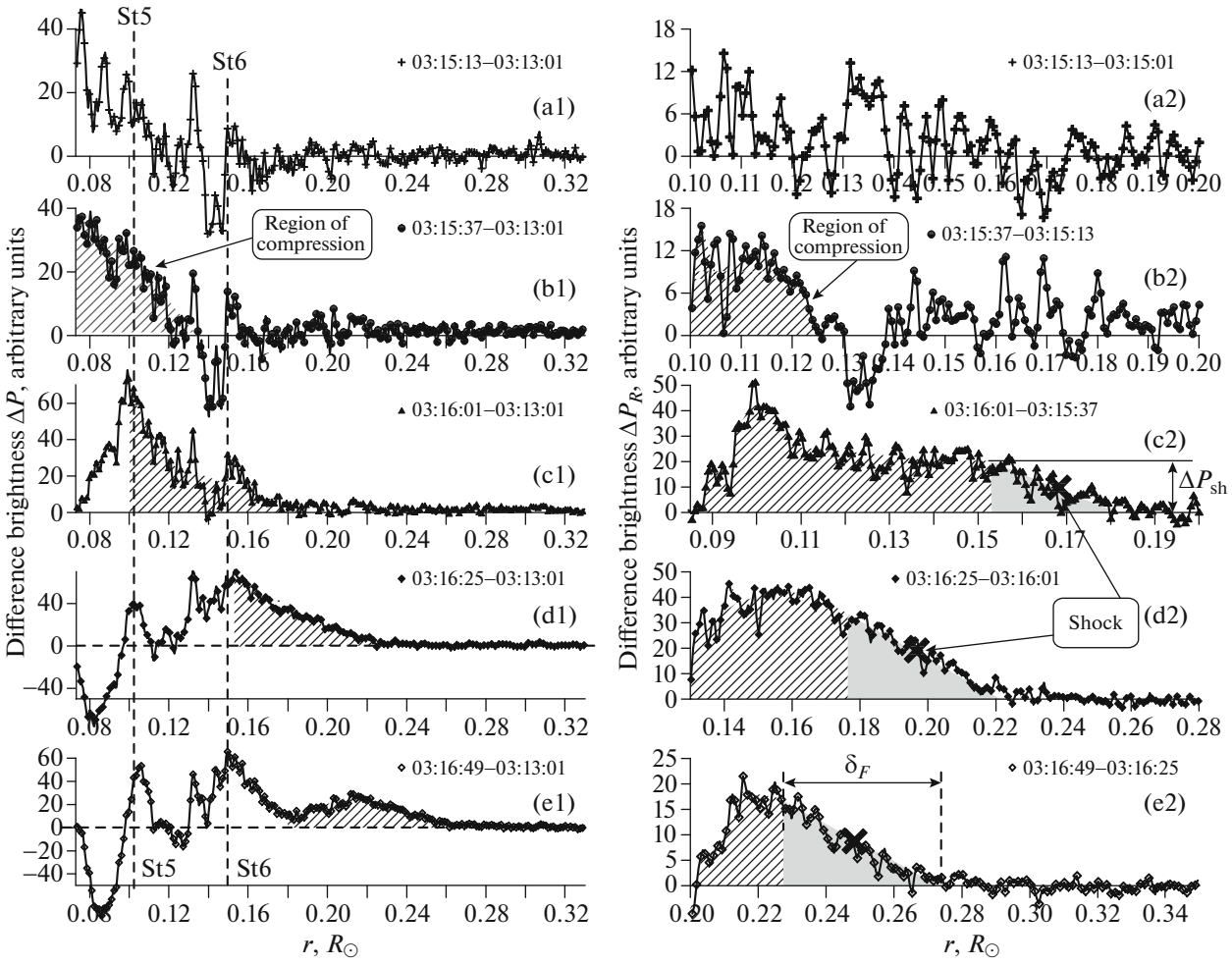

Fig. 3. AIA/SDO (a1)–(e1) difference brightnesses $\Delta P(r)$ and (a2)–(e2) running difference brightnesses $\Delta P_R(r)$ determined for SOL2012–10–23T03:13 in the 211 Å channel at times $t \geq 03:15:13$ UT. The other conditions are the same as those in Fig. 2.

3e1), but their positions remained almost the same. For all the ΔP profiles shown in Figs. 2c and 2d and Figs. 3a1–3e1, the peaks of the structures St4, St5, and St6 are located at almost fixed locations (shown by the vertical dashed lines).

Thus, these data indicate that this event does not display any formation of moving frontal CME structures that could act as pistons exciting regions of compression (perturbed zones) ahead of themselves or shocks. It is well known, in their motion in "impulsive" CMEs, similar arc structures catch up to each other and merge into a single moving structure that forms the frontal structure of the CME [20, 21].

4. ANALYSIS OF SOL2012–10–23T03:13 OBSERVED IN THE "HOT" 131 Å CHANNEL

In the event considered, the region of compression generated after $t = 03:15:13$ UT propagates away from the Sun, and this region could result from an impulsive action exerted on the ambient coronal plasma by the total pressure, which increases sharply in the flare region. To verify this hypothesis, we examined the running difference brightness detected in the "hotter" 131 Å channel. Figure 4 presents images of the running difference brightness for SOL2012–10–23T03:13 detected at similar times in the 211 Å (Fig. 4a) and 131 Å (Fig. 4b) channels. In the 131 Å channel, we can see the formation of the structure St1 at the point O and the three arc structures St2, St3, and St4, which display behavior similar to that observed in the 211 Å channel. At the same time, the structures St5 and St6, as well as the region of compression and the shock, are absent. This may indicate that these latter elements have lower temperatures than the value $T \approx 10^7$ K, typical for the 131 Å channel. In contrast, these structures are

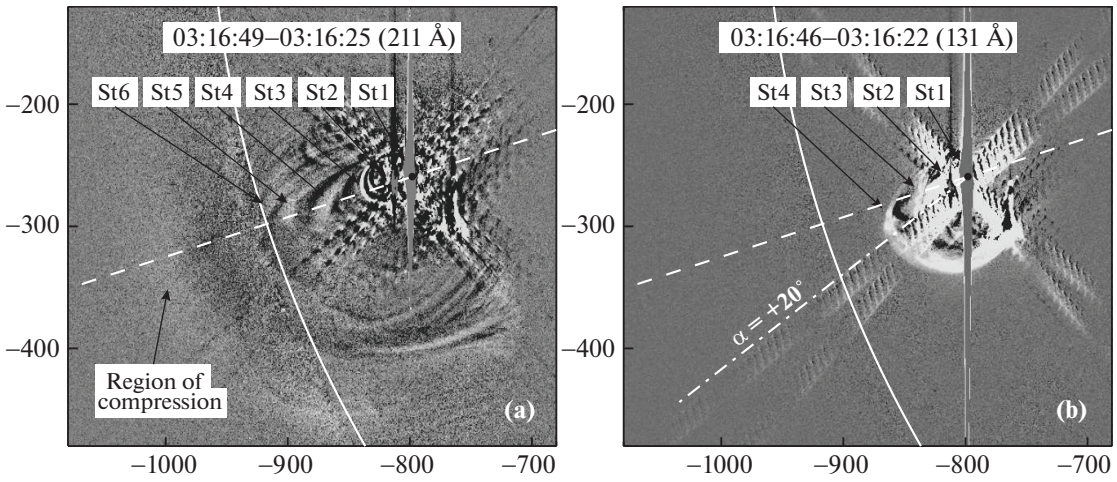

Fig. 4. AIA/SDO images of the running difference brightness detected in the (a) 211 Å and (b) 131 Å channels for SOL2012–10–23T03:13 at 03 : 16 : 49 UT and 03 : 16 : 46 UT, respectively. The axes indicate solar coordinates in arcseconds.

visible in the 211 Å channel, which corresponds to $T \approx 2 \times 10^6$ K.

We can study the dynamics of this event in more detail using distributions of the running difference brightness $\Delta P_R(r)$ detected in the 131 Å channel at successive times for $PA = 108°$, $R_C = 0.87\ R_\odot$, $\alpha = 20°$, and $\delta\alpha = 5°$ (see Figs. 5a–5c). The selected direction α corresponds to the direction of propagation of the leading portion of St4 observed in the 131 Å channel (see Fig. 4b). A visual analysis of the $\Delta P_R(r)$ profiles presented in Figs. 5a–5c shows that the temporal behavior of the structures St1, St2, and St3 observed in the 131 Å channel is similar to that of the $\Delta P(r)$ profiles observed in the 211 Å channel (see Figs. 2a and 2b). Initially, the maxima of their brightness peaks shift somewhat along r, but then remain almost fixed, though their brightness gradually decreases with time. The behavior of St4 observed in the 131 Å channel differs appreciably from that observed in the 211 Å channel. This is indicated by the time variations in the $\Delta P_R(r)$ profiles observed in the 131 Å channel and presented in Figs. 5a1–5c1 on enlarged scales.[4] Figure 5b1 shows (filled circles) that St4 becomes visible after 03:15:34 UT. Before this time, only St3 was observed, at $r \approx 0.033\ R_\odot$ (hollow circles in Fig. 5b1). The amplitude of St3 decreases somewhat at 03:15:58 UT (filled circles). The mean point of the leading portion of St4 (marked by × in Figs. 5b1 and 5c1) is located at $r \approx 0.058\ R_\odot$.

Afterwards, the leading portion of St4 moves with deceleration (see Figs. 5b1 and 5c1), while its brightness amplitude ΔP_L decreases almost to the noise level (see Fig. 5b1) at a distance of $r \approx 0.13\ R_\odot$, reached at time 03:23:10 UT (not shown in Fig. 5). Recall that, after a small shift, the St4 peak observed in the 211 Å channel remained almost fixed at $r \approx 0.065\ R_\odot$, with its amplitude decreasing with time (see Figs. 2b and 2d). We can examine the spatial and temporal dynamics of the observed structures and the shock front more clearly using the kinematic curves presented in Figs. 6a and 6b.

Figure 6a presents the kinematics of the motion of St1–St4 observed in the 211 Å channel. As was noted above, each structure first undergoes acceleration and related motion, but then stops at its individual distance r from the point O. We can also see that the beginning of the St2–St4 acceleration describes a single trajectory (dashed), attributed to the action of some external agent. This trajectory is constructed in Fig. 6b (pluses) using the circled points in Fig. 6a. As was noted above, all the structures St1–St4 are also visible in the "hot" 131 Å channel (see Fig. 4b).

The kinematic curve (filled circles in Fig. 6b) constructed for the mean point (marked by × in Figs. 5b1 and 5c1) of the leading portion of St4 observed in the 131 Å channel is a reasonable extension of the St2–St4 trajectory (circles in Fig. 6b) observed in the 211 Å channel. Namely, this curve (filled circles in Fig. 6b) provides a fairly good description of the motion and expansion of the bright boundary St4 observed in the hot 131 Å channel (see Fig. 4b). The trajectory of the mean point of the leading front of the region of compression (marked by × in Figs. 3c2–3e2) observed in the 211 Å channel and imagined to be a shock front, with its velocity decreasing with time, is shown by the squares in Fig. 6b. The time dependence for the shock front (hollow circles in Fig. 6b)

[4] It was already noted that St5 and St6, as well as the region of compression and shock, are not visible in the 131 Å channel

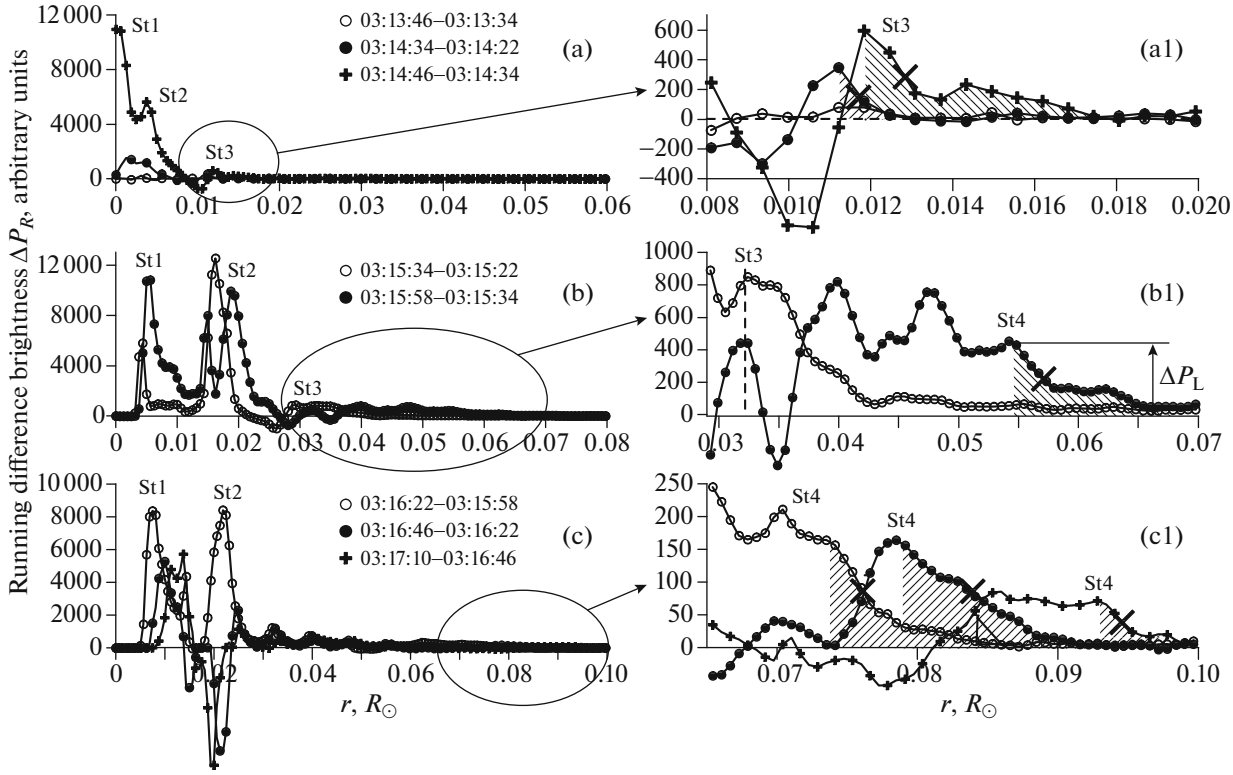

Fig. 5. AIA/SDO distributions of the running difference brightness $\Delta P_R(r)$ detected in the 131 Å channel at successive times during SOL2012–10–23T03:13. The distributions were constructed in the direction $\alpha = 20°$ from the initial point O ($PA = 108°$, $R_C = 0.87\ R_\odot$) and with angular averaging over $\delta\alpha = 5°$. Images (a)–(c) and (a1)–(c1) correspond to identical times, but are shown for different spatial scales.

was fitted by a second order polynomial (parabola). Figure 6e presents the time derivatives of both curves, with these derivatives being the speeds of the structure St4 and the shock. Two important questions arise in this connection:

1. Is the leading front of the region of compression a real shock?

2. What is the reason for the shock excitation if no CME is observed?

5. BASIS FOR THE EXISTENCE OF A SHOCK FRONT IN SOL2012–10–23T03:13. COMPARED WITH THE SIMILAR EVENT SOL2011–02–28T07:34

To demonstrate the generation of a shock front in our case, we used results obtained earlier for piston shocks excited in the fronts of CMEs. A method for the detection and identification of piston shock fronts moving ahead of CMEs in various directions relative to the axis of the CME motion observed at distances $R < 30\ R_\odot$ from solar center was proposed in [11, 22]. The concept of a perturbed zone excited in front of a CME, which affects the unperturbed solar wind, provides the physical basis for the method [13]. When the CME velocity u relative to the unperturbed solar wind exceeds the local magnetosonic speed, which is approximately equal to the Alfven speed V_A in the solar corona, a shock is formed in the leading portion of the perturbed zone [22]. It was also shown that, at distances $R < 6\ R_\odot$, the shock front width δ_F is comparable to the mean free path of protons λ_p, and the mechanism of the shock-energy dissipation is collisional [22]. This indicates that δ_F increases as $\sim 1/N(R)$, depending on the distance from the Sun, where N is the number density of the unperturbed coronal plasma [23].

Turning to our case without a CME, we note that the region of compression shown by slanted shading in Figs. 3b–3e is an analog of a perturbed zone. The only difference is that perturbed zones are formed under the continuous action of CME pistons, whereas the region of compression generated by a yet unknown impulsive pressure moves without taking energy from any pistons, but rapidly decaying. The shock front in the leading portion of the region of compression was first detected at 03:16:01 UT at a distance $r \approx 0.17\ R_\odot$ from the point O (see Fig. 3c2). The initial shock velocity projected onto the plane of the sky within distances $r \approx 0.17–0.25\ R_\odot$ was

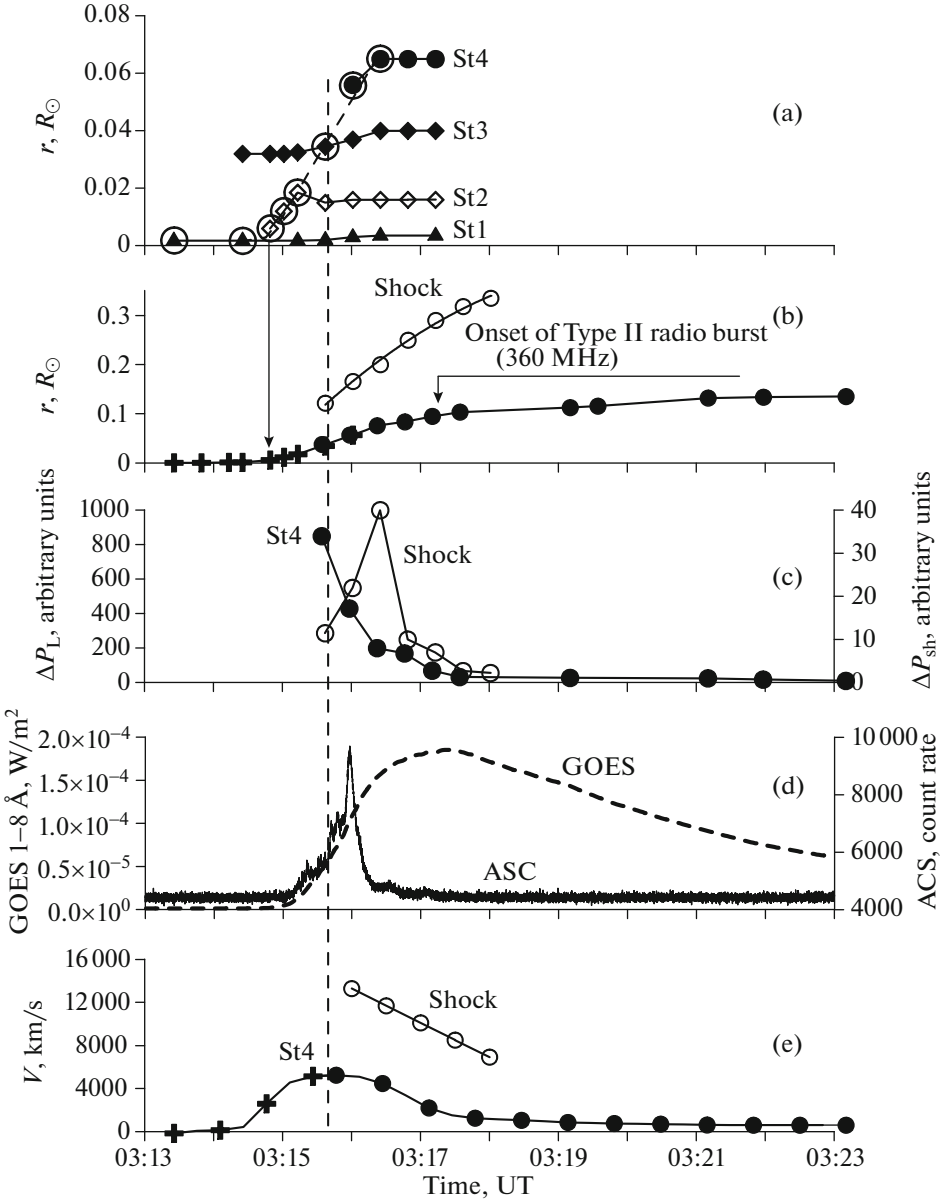

Fig. 6. Distance r determined as a function of time for SOL2012−10−23T03:13, measured in the direction of $PA = 108°$ from the point O located at $R_C = 0.87\ R_\odot$. (a) Maxima of the difference brightness ΔP_{max} (shown by vertical dashed lines in Figs. 2 and 3) of the structures St1 (▲), St2 (◊), St3 (♦), and St4 (●) detected in the 211 Å channel. (b) Maxima of the difference brightness ΔP_{max} of the structures St1 and St2 (+) circled in Fig. 6a, the mean points of the shock front (○) corresponding to × shown in Figs. 3b2–3e2, and the mean points of the leading portion of the structure St4 detected in the AIA/SDO 131 Å channel (●), corresponding to × shown in Figs. 5b1–5c1. (c) Jumps ΔP_L (see Fig. 5b1) in the running difference brightness for the leading portion of the structure St4 detected in the 131 Å channel (●) and jumps ΔP_{sh} (see Fig. 3c2) in the shock front detected in the AIA/SDO 211 Å channel (○). (d) GOES X-ray fluxes detected in the 1–8 Å channel (dashed curve) and ACS/INTEGRAL (>100 keV) count rates (solid). (e) Speeds of the structure St4 (●) and the shock front (○) constructed as time derivatives of the curves presented in Fig. 6b.

$V_r \approx 1200$ km/s (see Figs. 3c2–3e2). At distances $r \approx 0.25\ R_\odot$ ($R \approx 1.3\ R_\odot$), the shock front width was $\delta_F \approx 0.05\ R_\odot$ (see Fig. 3e2). According to [22], the Alfven speed at these distances is $V_A < 800$ km/s, so that the main condition for shock excitation is fulfilled. The detected width of the front δ_F nearly corresponds to the width of the collisional piston shock detected at distances $R \approx 1.3$–$1.4\ R_\odot$ or altitudes $h \approx 0.3$–$0.4\ R_\odot$ (see [22, Fig. 5b]). This nearly fits our case, where $h \approx r/\sin(\Phi) \approx 0.25/\sin(58°) \approx 0.3\ R_\odot$ and Φ is the heliographic longitude of the origin of the flare or St1. All the facts presented above

support our idea that the front of the leading portion of the region of compression shown in Figs. 3c2–3e2 is a collisional shock. In addition, we also note the following.

1. The shock front appears simultaneously with a rapid increase in the hard X-ray flux from the flare (vertical dashed lines in Figs. 6b and 6d); the flux of soft X rays reaches its maximum about 1.5 min later.

2. A Type II radio burst that is obviously related to the shock-front propagation is observed, although its first appearance was detected at 03:17:25 UT, about 1.5 min later than the first appearance of the shock front in the 211 Å channel (see Fig. 6b).

These two facts were also observed in SOL2011–02–28T07:34, which is similar to SOL2012–10–23T03:13 in the absence of a CME [1]. In that case, the generation of a shock front in the absence of a CME was supported by the detected time dependence of the shock velocity $V(t)$ compared to the temporal drift in the frequency of the Type II radio burst. We used this technique to obtain additional verification of our conclusion concerning the shock.

Recall that the theory [24] associates Type II radio bursts with fluxes of energetic particles (electrons and ions) moving through rarefied plasma, with these particles being able to excite electrostatic oscillations at the electron plasma frequency. These oscillations can then be transformed into the first (fundamental) F and second H harmonics of the radio emission via Rayleigh and Raman scattering, respectively.

Assuming radial propagation of the source of the Type II radio burst, we can estimate the function $V(r)$ and compare this with the observed shock velocity dependence $V_{sh}(r)$. To obtain this estimate, we used the relation between the fundamental (plasma) frequency of the radio emission and the local electron density of the region producing the emission

$$F = 9 \times 10^{-3}\sqrt{n(r)}, \qquad (1)$$

where F is the fundamental frequency in MHz and n is the number of electrons per cubic centimeter. The detected harmonic frequency is $H = 2F$. We can take the distribution $n(r)$, in particular, from the model [25].

In SOL2012–10–23T03:13, the e-Callisto SSRT radio spectrometer detected a Type II radio burst at the main frequency F and second harmonic $H \approx 2F$ (see Fig. 7a). Both harmonics were split in two components f_1 and f_2. A drift of the radiation at the H harmonic from ≈370 MHz to ≈110 MHz over ≈4 min was observed (the interval following 03:19:00 UT is not shown in Fig. 7a). A frequency drift in F is clearly visible over a shorter time interval. Since the frequency drift in F is clearer than the drift in H, we used the former curves, assuming $F = (f_1 + f_2)/2$ (see Fig. 7a). The time dependence for the heights of the shock front above the solar surface, $h \approx r/\sin(\Phi) \approx r/\sin(58^\circ)$, is shown by the circles in Fig. 7b. The last detected position of the front, $h \approx 0.4\ R_\odot$, corresponds to the onset of the radio burst observed at 03:18:00 UT at $F \approx 140$ MHz (see Fig. 7a), though the burst in the H harmonic had been observed starting from 03:17:00 UT. The model number density of the coronal plasma n [25] multiplied by a coefficient of 5.5 corresponds to the frequency $F \approx 140$ MHz at height $h \approx 0.4\ R_\odot$. Assuming such a distribution for $n(R)$, Fig. 7a presents the drift in the frequency F (as well as in f_1 and f_2) calculated from the shock-front trajectory within the single time interval 03:15:30–03:18:00 UT, shown by hollow circles in Fig. 7b (the indicated errors were determined as the half-widths of the shock front). The function $h(t)$ calculated from the drift curve $F(t)$ (squares in Fig. 7a) is shown by squares in Fig. 7b for $t \gtrsim$ 03:18:00 UT. We fitted the derived trajectory $h(t)$ with a parabola, with its time derivative shown in Fig. 7c as the velocity $V_{sh}(t)$. The results obtained applying these assumptions indicate a connection between the Type II radio burst and the shock-front propagation.

Type II radio bursts in the absence of CMEs are observed fairly rarely. The event of this type that was considered in greatest detail is SOL2011–02–28T07:34, studied in [1]. In that case, the shock was not directly detected, but visual identifications of a moving boundary with a slightly enhanced brightness visible in the AIA/SDO difference brightness images obtained in the 171 Å, 193 Å, and 211 Å channels were used. Therefore, the relation established between the frequency drift in the Type II burst and the velocity of the moving boundary was used to identify the boundary as a shock front. In order to verify the conclusions of [1], we applied our method for the direct detection and identification of shock fronts to SOL2011–02–28T07:34. Here, we must take into account that the front was first observed above the limb at about 07:38:44 UT. Figure 8a shows the running difference brightness image in the 193 Å channel constructed for 07:39:32 UT, with the region of compression above the limb indicated. The position angle $PA = 54^\circ$ of the propagation of the leading portion of this region and the point O located at a distance $R_C = 0.78\ R_\odot$ from the solar center are visible, as well as the angle α indicating the direction in which the running difference brightness ΔP_R was constructed. Following [1], we assumed that the propagation occurs close to the plane of the sky, and examined the motion of the region of compression and of the front as functions of R, i.e., of the distance from the solar center.

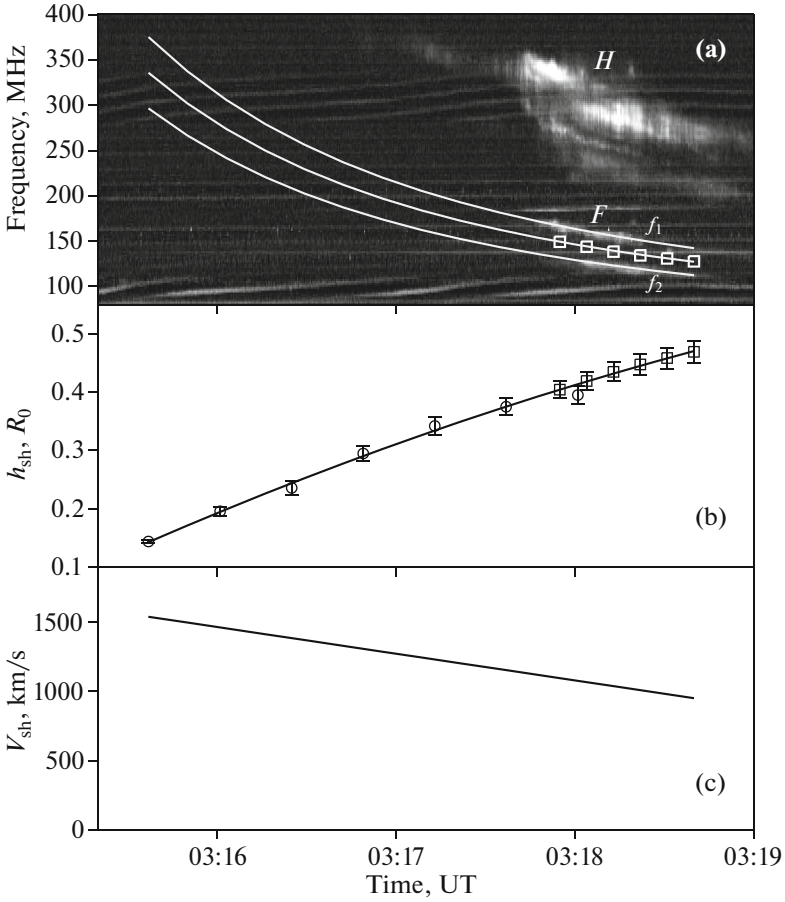

Fig. 7. (a) The e-Callisto (SSRT) Type II radio bursts detected for SOL2012–10–23T03:13 at the fundamental frequency F and the second harmonic H. Each frequency is split into two close frequencies f_1 and f_2. (b) Experimental altitudes $h \approx r(t)/\sin 58^\circ$ of the mean point of the shock front above the solar surface (circles), which correspond to the $\times$ shown in Figs. 3c2–3e2, and the function $h(t)$ (squares) calculated from the drift in the fundamental frequency $F(t)$ for $t \gtrsim$ 03:18:00 UT, assuming that the coronal plasma density $n(r)$ at these altitudes is described by the model [25] with the coefficient 5.5. (c) The function $V(t)$ of the front velocity calculated by differentiating the curve shown in Fig. 7b.

Figures 8b–8e present distributions of the running difference brightness ΔP_R detected in the 193 Å channel and constructed for $PA = 54^\circ$, $R_C = 0.78\ R_\odot$, $\alpha = 10^\circ$, and $\delta\alpha = 5^\circ$ as functions of the distance R from the center of the Sun at successive times. The the region of compression (shown by slanted shading) was first detected at 07:39:32 UT (see Fig. 8c). The shock front is shown in gray. At distances $R_C < 1.2\ R_\odot$, the front width δ_F remains almost constant and reaches $(2–3)L$, where $L = 0.0013\ R_\odot$ is the SDO/AIA spatial resolution. This is fully expected, due to the high noise level in and behind the region of the front (see Figs. 8c–8e).

The generation of the region of compression was accompanied by a high-temperature *jet* (see Fig. 8a). Figure 9a presents kinematic curves for the leading portion of the jet (filled circles) and for the mean point of the shock front (hollow circles). The appearance of the jet precedes the generation of the region of compression and shock; the speed of the leading portion of the jet (filled circles in Fig. 9c) first sharply increases, then decreases synchronously with a drop in the brightness jump at its leading portion (filled circles in Fig. 9b). The shock continues its propagation with successively decreasing speed (straight line in Fig. 9c). The true velocity of the shock front could be somewhat higher, if the motion of the region of compression and of the front does not lie strictly in the plane of the sky.

Similarly to SOL2011–02–28T07:34, the event SOL2012–10–23T03:13 was preceded by significant changes in the photospheric magnetic field in the parent active region (see Fig. 10), detected by the HMI/SDO vector magnetograph [26]. This was most clearly manifest as a strengthening of the positive vertical magnetic field (Fig. 10c). Some smaller changes in the horizontal magnetic field were also

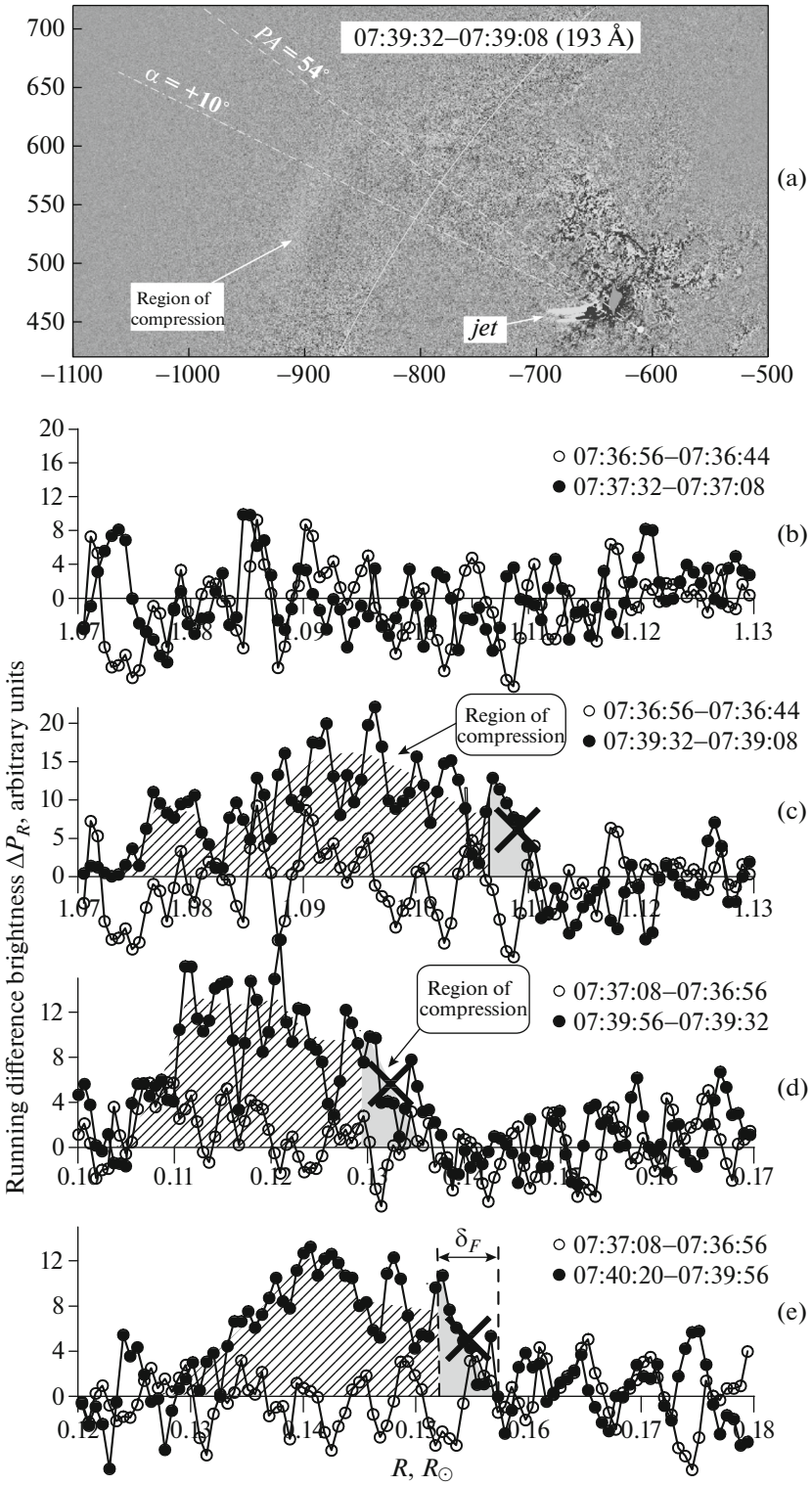

Fig. 8. (a) AIA/SDO image of the running difference brightness detected for SOL2011–02–28T07:34 at 07:39:32 UT in the 193 Å channel. (b)–(e) Running difference brightness profiles ΔP_R constructed for successive times and for $PA = 54^\circ$, $R_C = 0.78\ R_\odot$, $\alpha = 10^\circ$, and $\Delta\alpha = 5^\circ$, as functions of the distance R from the solar center.

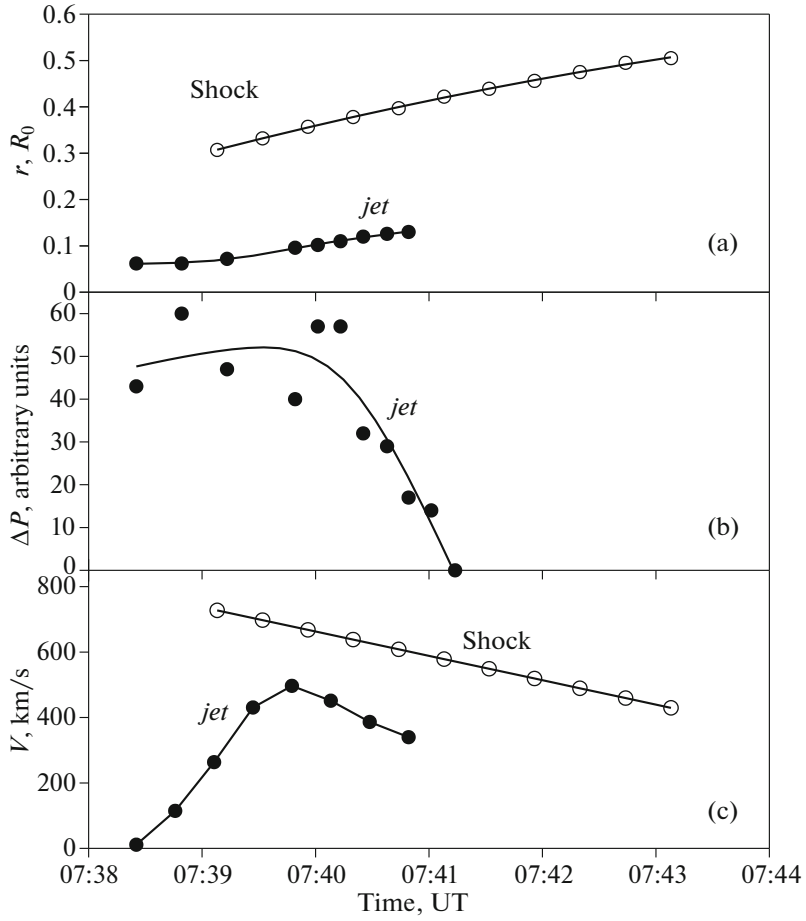

Fig. 9. Time dependences indicated by the AIA/SDO data obtained for SOL2011–02–28T07:34, for (a) the distance r of the mean point of the shock front (hollow circles) in the 193 Å channel, marked by × in Figs. 8b–8e, and for the mean point of the leading portion of the *jet* (filled circles) detected in the 171 Å channel, with both functions constructed for $R_C = 0.78\ R_\odot$, $\alpha = 30°$, and $\Delta\alpha = 10°$); (b) the jump in the running difference brightness for the leading portion of the *jet* revealed in the 171 Å channel; (c) the speed of the shock front (hollow circles) and of the *jet* (filled circles) constructed by differentiating the curves shown in Fig. 9a.

observed (Fig. 10b). The vertical electric currents did not show any appreciable changes (Figs. 10e and 10f)

On the whole, the scenario for SOL2011–02–28T07:34 is similar to that for SOL2012–10–23T03:13. Therefore, discussing the generation of the region of compression and shock in SOL2012–10–23T03:13, we will follow the discussion on SOL2011–02–28T07:34 presented in [1].

6. DISCUSSION

Similar to a number of other studies (for example [27]), it is noted in [1] that magnetic flux emerging from the convective zone was detected in the region of flare generation. This suggests that the event SOL2011–02–28T07:34 results from reconnection between an emerging magnetic loop and an inclined coronal magnetic loop with both bases rooted in the photosphere. Due to the reconnection with the emerging magnetic flux, under the influence of the tension in the field lines, the coronal loop first sharply expands and then quickly stops, generating a shock. The dynamics of the hot *jet* moving with the loop supports this idea (Fig. 9). When the loop's expansion is stopped, the shock propagates farther without the action of any piston. This is believed to be a new mechanism for shock generation. The shock is formed by a transient piston effect, since the coronal loop does not erupt, in contrast to cases accompanied by CMEs.

Returning to SOL2012–10–23T03:13, we note that a bright region observed in the hot 131 Å channel and bounded by the arc structure St4 shown in Fig. 4b is similar to the hot jet observed in SOL2011–02–28T07:34. Indeed, the speed of this region first sharply increases, then quickly drops almost to zero

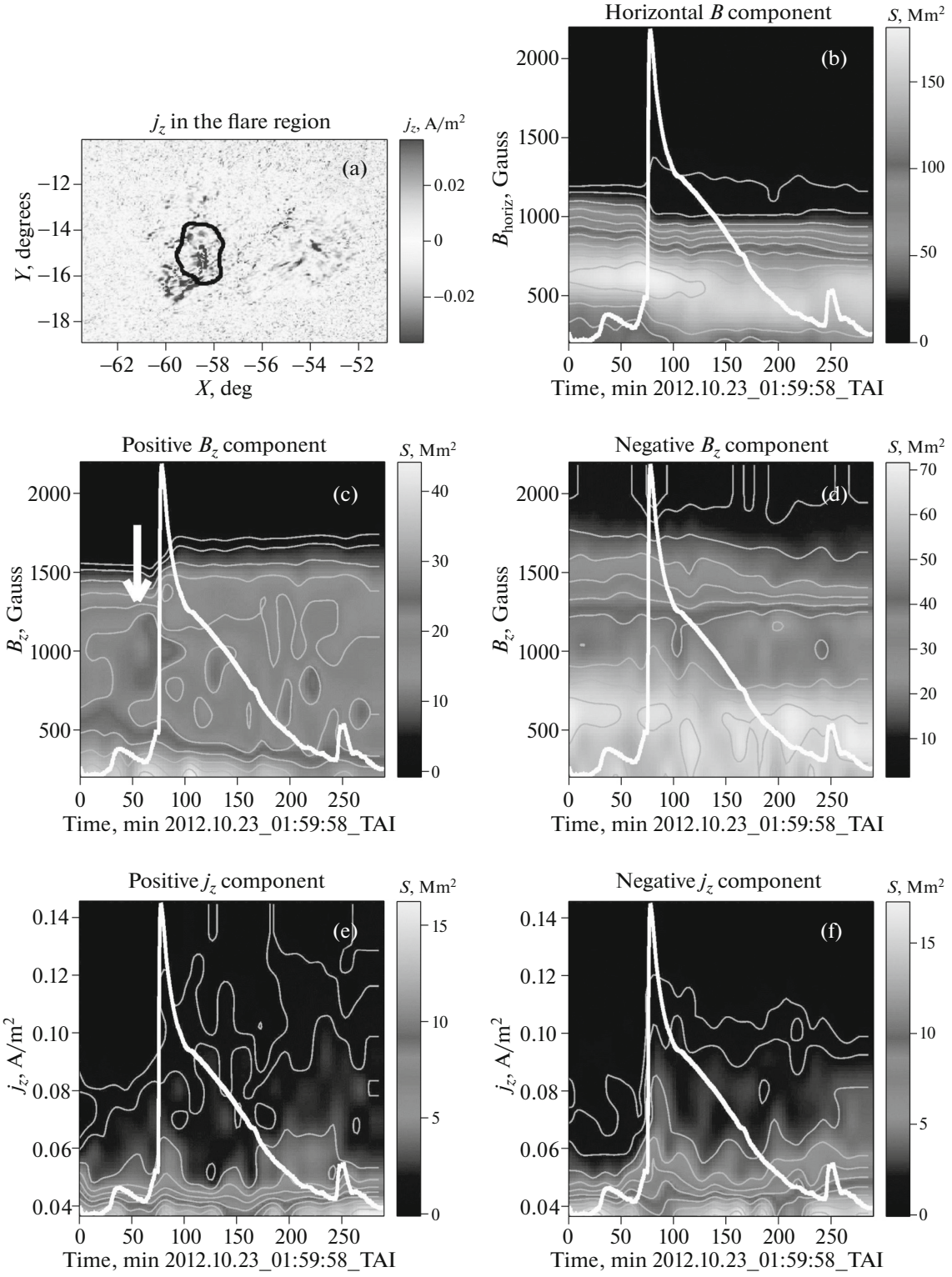

Fig. 10. HMI/SDO photospheric variations in the magnetic fields and vertical electric currents of the parent active region for SOL2012–10–23T03:13: (a) map of the vertical electric currents (the bold contour indicates the region whose characteristics are shown in the remaining plots); total areas of pixels with the indicated (b) horizontal, (c) positive vertical, and (d) negative vertical magnetic fields (the downward arrow in Fig. 10c shows the most prominent change in the magnetic field preceding the event); total areas of pixels with the indicated densities of (e) positive and (f) negative vertical currents (the bold white curve in Figs. 10b–10f show the GOES time profile for the soft X-ray flux from the flare detected in the 1–8 Å channel).

(filled circles in Fig. 6c and the dashed curve in Fig. 6e), with a simultaneous drop in brightness (filled circles in Fig. 6c). This generates a shock that continues to propagate, with its speed decreasing after the jet stops (hollow circles in Fig. 6c and the solid curve in Fig. 6e). In our case, the jet differs mainly in its size and form. It may be that our situation is more complex, with an emerging magnetic rope instead of a magnetic loop, which successively interacts with coronal magnetic loops standing in its path.[5] When the orientations of the magnetic fields of the rope and surrounding loops of the parent active region are opposite, magnetic reconnection can bring about rapid heating of the rope and an increase in its pressure [28, 29]. This pressure increase can result in a sharp expansion of the rope and its impulsive action on other surrounding loops, leading to the rope's deceleration. This can generate a shock, which continues to propagate and then decays without the action of a piston. The appearance of bursts of hard X rays radiated by accelerated electrons shortly before the appearance of the shock front (Figs. 6b–6d) also suggests a magnetic-reconnection process initiated by an interaction between a rope and coronal loops [30].

Thus, similarly to SOL2011–02–28T07:34, the generation of the shock front in SOL2012–10–23T03:13 may also be associated with the transient (impulsive) effect of a magnetic piston (rope), though the origin of this piston is unclear and could be quite different. This requires additional studies which go beyond the scope of the present work.

7. CONCLUSIONS

1. In the solar event SOL2012–10–23T03:13 considered here, there was no CME, but a Type II radio burst was observed.

2. Our direct detection of profiles of the difference brightness in the AIA/SDO 211 Å channel reveals the formation and propagation of a region of enhanced brightness (and probably of compression), with a collisional shock detected in front of this region at distances $R < 1.3\ R_\odot$ from the center of the Sun.

3. We suggest that the origin of this region of compression and shock is a transient (impulsive) action exerted on the surrounding plasma by an eruptive, high-temperature magnetic rope. The initial instability of this rope may have resulted from interactions with the emerging magnetic flux, while its heating and initial acceleration could result from magnetic reconnection.

4. The absence of any CME may indicate that the eruption of the magnetic rope was stopped at a height of ≈0.1 $R_\odot$ (≈70 Mm) above the photosphere, due to the rope's interaction with surrounding coronal loops.

[5] Magnetic ropes differ from loops in their field components transverse to the loop axis.

ACKNOWLEDGMENTS

This work was supported by the Russian Foundation for Basic Research (projects 15-32-21078-young-a-leading and 16-32-00462-young-a). The authors are grateful to the teams maintaining the AIA/SDO, HMI/SDO, ACS/INTEGRAL, GOES, and SSRT/Callisto instruments for the data used in this study.

REFERENCES

1. W. Su, X. Cheng, M. D. Ding, P. F. Chen, and J. Q. Sun, Astrophys. J. **804**, 88 (2015).
2. E. W. Cliver, N. V. Nitta, B. J. Thompson, and J. Zhang, Solar Phys. **225**, 10 (2004).
3. Y. Liu, J. G. Luhmann, S. D. Bale, and R. P. Lin, Astrophys. J. **691**, L151 (2009).
4. P. F. Chen, Liv. Rev. Solar Phys. **8**, 1 (2011).
5. K.-S. Cho, N. Gopalswamy, R.-Y. Kwon, R.-S. Kim, and S. Yashiro, Astrophys. J. **765**, 148 (2013).
6. Y. Leblanc, G. A. Dulk, A. Vourlidas, and J.-L. Bougeret, J. Geophys. Res. **106**, 25301 (2001).
7. J. Magdalenić, B. Vrsnak, S. Pohjolainen, M. Temmer, H. Aurass, and N. J. Lehtinen, Solar Phys. **253**, 305 (2008).
8. A. Nindos, C. E. Alissandrakis, A. Hillaris, and P. Preka-Papadema, Astron.Astrophys. **531**, A31 (2011).
9. V. V. Zheleznyakov, *Radio Emission of the Sun and Planets* (Pergamon, Oxford, 1970).
10. N. Gopalswamy, W. T. Thompson, J. M. Davila, M. L. Kaiser, et al., Solar Phys. **259**, 227 (2009).
11. M. V. Eselevich and V. G. Eselevich, Geophys. Res. Lett. **35**, L22105 (2008).
12. M. V. Eselevich and V. G. Eselevich, Astron. Rep. **55**, 1038 (2011).
13. M. V. Eselevich and V. G. Eselevich, Astron. Rep. **51**, 947 (2007).
14. M. V. Eselevich, Astron. Rep. **54**, 173 (2010).
15. V. G. Eselevich, M. V. Eselevich, and I. V. Zimovets, Astron. Rep. **57**, 142 (2013).
16. A. Kerdraon and J.-M. Delouis, *Coronal Physics from Radio and Space Observations,* Ed. by G. Trottet (Springer, 1997), p. 192.
17. V. G. Eselevich, M. V. Eselevich, and I. V. Zimovets, Astron. Rep. **60**, 163 (2016).
18. J. Magdalenić, C. Marqué, A. N. Zhukov, B. Vršnak, and A. Veronig, Astrophys. J. **746**, 152 (2012).
19. J. R. Lemen, A. M. Title, D. J. Akin, P. F. Boerner, et al., Solar Phys. **275**, 17 (2012).
20. V. G. Eselevich and M. V. Eselevich, Astron. Rep. **57**, 860 (2013).

21. V. G. Eselevich, M. V. Eselevich, I. V. Zimovets, and G. V. Rudenko, Astron. Rep. **60**, 1016 (2016).
22. V. Eselevich and M. Eselevich, Astrophys. J. **761**, 68 (2012).
23. Yu. B. Zel'dovich and Yu. P. Raizer, *Physics of Shock Waves and High-Temperature Hydrodynamic Phenomena* (Nauka, Moscow, 1966; Academic, New York, 1966, 1967).
24. Z. Kuncic, I. H. Cairns, S. Knock, and P. A. Robinson, Geophys. Res. Lett. **29**, 2 (2002).
25. G. Newkirk, Jr., Astrophys. J. **133**, 983 (1961).
26. P. H. Scherrer, J. Schou, R. I. Bush, A. G. Kosovichev, et al., Solar Phys. **275**, 207 (2012).
27. M. A. Livshits, I. Yu. Grigoryeva, I. I. Myshyakov, and G. V. Rudenko, Astron. Rep. **60**, 939 (2016).
28. Y. Fan and S. E. Gibson, Astrophys. J. **641**, L149 (2006).
29. R. F. Pinto, N. Vilmer, and A. S. Brun, Astron. Astrophys. **576**, A37 (2015).
30. S. A. Kuznetsov, I. V. Zimovets, A. S. Morgachev, and A. B. Struminsky, Solar Phys. **291**, 3385 (2016).

Translated by V. Badin